Remote Sensing Applications: Society and Environment 35 (2024) 101230

Contents lists available at ScienceDirect

Remote Sensing Applications: Society and Environment

journal homepage: www.elsevier.com/locate/rsase

Harmonized NDVI time-series from Landsat and Sentinel-2 reveal phenological patterns of diverse, small-scale cropping systems in East Africa

Adomas Liepa [a,*], Michael Thiel [a], Hannes Taubenböck [b,c], Ingolf Steffan-Dewenter [d], Itohan-Osa Abu [a], Maninder Singh Dhillon [a], Insa Otte [a], Michael Hilary Otim [e], Moses Lutaakome [e], David Meinhof [d], Emily A. Martin [f], Tobias Ullmann [a]

[a] *Earth Observation Research Cluster, Department of Remote Sensing, Institute of Geography and Geology, University of Würzburg, 97074, Würzburg, Germany*
[b] *Earth Observation Research Cluster, Department of Global Urbanization and Remote Sensing, Institute of Geography and Geology, University Würzburg, 97074, Würzburg, Germany*
[c] *German Aerospace Center (DLR), German Remote Sensing Data Center (DFD), Oberpfaffenhofen, Germany*
[d] *Department of Animal Ecology and Tropical Biology Biocentre, University of Würzburg, 97074, Würzburg, Germany*
[e] *National Crops Resources Research Institute (NaCRRI), Namulonge. National Agricultural Research Organization, Kampala, P.O. Box 7084, Uganda*
[f] *Department of Animal Ecology & Systematics, Justus Liebig University of Gießen, 35392, Gießen, Germany*

ARTICLE INFO

Keywords:
Agriculture
Harmonization
East africa
Remote sensing

ABSTRACT

Capturing the phenological responses of crops in diverse, small-scale agricultural systems is one of the most notable remote sensing research gaps in Eastern Africa. Because of the heterogeneous and complex agricultural environments, remote sensing methodologies successfully implemented elsewhere yield poor results in Eastern Africa. The reliance on local rainfall and dry spells can lead to alterations in planting patterns, impacting growing season timing and yield, underscoring the importance of high temporal resolution for capturing crop phenology. We generated a high-resolution land use/land cover (LULC) classification map of 10 m using Sentinel-1 and Sentinel-2 imagery together with a large set of reference data acquired in situ in 2022. The LULC classification yielded an overall accuracy of 87.9% and Cohen's kappa value of 0.83. Based on the LULC map, we investigated the phenological metrics of the most important crops in the Kamuli district of Eastern Uganda by combining a multi-sensor harmonization approach, thresholding method, and cloud computing. Previously unavailable Landsat 9 band adjustment coefficients were derived. By harmonizing Landsat (LS) 7 Enhanced Thematic Mapper Plus (ETM+), Landsat 8 and 9 Operational Land Imager (OLI), with Sentinel-2 Multispectral Instrument (MSI), the phenological patterns during the March to May growing season were captured using a dense temporal Normalized Difference Vegetation Index (NDVI) time series. The seasonal onset for most crop types was in the end of March to middle of April while the end of the growing season occurred from the end of June to middle of July. Investigation of the 13 crop types using a high-resolution LULC map and dense, harmonized NDVI time series signifies the first field-level phenological metrics estimation of smallholder farming systems in Eastern Africa. Future research should focus

* Corresponding author.
E-mail address: adomas.liepa@uni-wuerzburg.de (A. Liepa).

https://doi.org/10.1016/j.rsase.2024.101230
Received 2 October 2023; Received in revised form 28 February 2024; Accepted 7 May 2024
Available online 10 May 2024

on expanding the methodology in space and time to provide insights into past and current growing season development.

1. Introduction

Vegetation phenology can be described as the timing of seasonal plant growth stages such as leaf development, flowering, senescence, and dormancy (Rathcke and Lacey 1985). Research on vegetation phenology provides vital information on multiple levels. On an environmental level, vegetation phenology acts as an indicator of climate variability and the extent to which the climate affects plants. In addition, the seasonal timing and duration of vegetation phenology governs local carbon intake, water balance and surface albedo (Fitchett et al., 2015). On a societal level, information on crop phenology can be employed to make informed decisions on land use management, application of nutrients and water distribution (Imeson and Prinsen 2004; Chen et al., 2007). In regions like East Africa, characterized by a succession of variable rainfall and dry spell events, and a strong dependency on agriculture for subsistence, understanding and capturing phenological patterns of crops within and between growing seasons is an essential component of adaptive strategies for climate change resilience.

Precipitation and temperature are primary drivers of the development of the growing season from onset to dormancy (Badeck et al.,

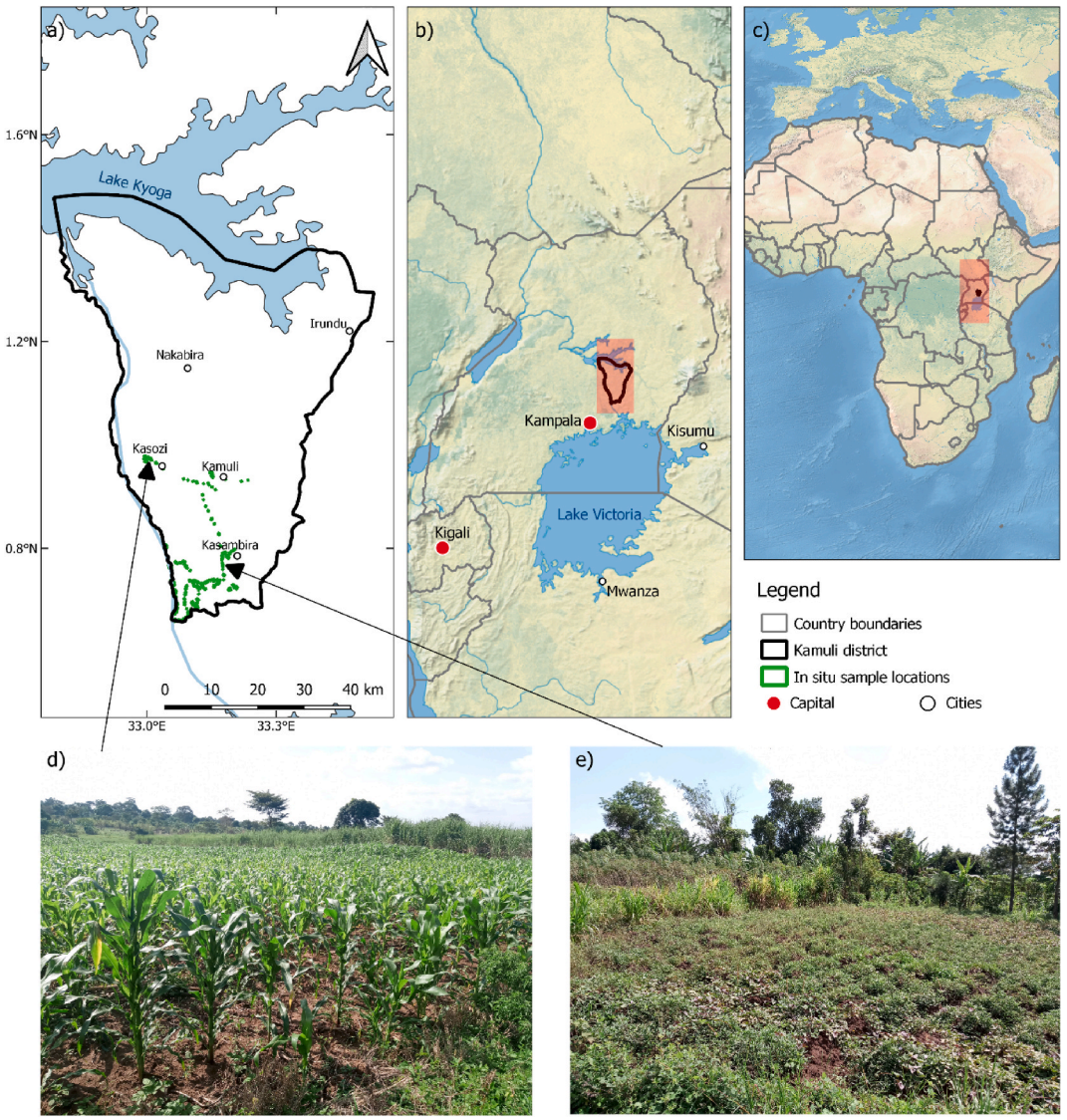

Fig. 1. Overview of the study area. The district boundary is visible in subplot a), country of Uganda boundary b), continental boundary c), maize monocrop d) and sweet potato e) fields in the study area. The images of the fields were taken during the field campaign in July 2022. Maps created with Natural Earth vector and raster map data at naturalearthdata.com.

2004; Reyer et al., 2013). East African cropping systems are characterized by a rapid response to rainfall events and local dry spells (Cheng et al., 2020). Abrupt variations in these parameters can cause shifting of planting patterns which in turn affect growing season duration, timing, and yields. From a remote sensing perspective, obtaining a dense cloud-free series of images is essential to accurately depict the local phenology.

Satellite remote sensing provides an effective data source to monitor phenological changes by measuring leaf reflectance (White et al., 2005; Zeng et al., 2020). Spectral responses in the near-infrared and visible red spectra can be used to calculate the Normalized Difference Vegetation Index (NDVI), a frequently used proxy for vegetation greenness. NDVI can track the rapid increase and decrease in surface greenness associated with the start and end of plant growing seasons (Pettorelli et al., 2005; Zhang et al., 2013). The maximum NDVI value can be used to identify the intensity of the peak vegetative stage. The start, end, and duration of the growing season together with the maximum greenness serve as the fundamental phenological metrics used to understand the temporal development of cropping systems during the growing season (Reed et al., 1994; Zeng et al., 2020).

The precise recording of the crop phenology has long been constrained by temporal and spatial resolution of satellite imagery (Fitchett et al., 2015; Cheng et al., 2020; Mananze et al., 2020). Several methods were developed to reduce these constraints: Vogels et al. (2019) combined Sentinel-2 NDVI time series with field-level segmentation and monthly land use maps to discriminate irrigated and rainfed agricultural systems. The combination of several satellite sensors has been explored by combining PlanetScope and Sentinel-2 data to examine phenology of short growing seasons in Kenyan rangeland (Cheng et al., 2020). The utility of Synthetic Aperture Radar (SAR) from Sentinel-1 to monitor phenology has been explored due to the insensitivity of SAR to cloud cover. Combining Sentinel-2 NDVI and Sentinel-1 backscatter by applying random forest regression technique showed high reliability for soybeans and maize monitoring in Western Bahia, Brazil (Filgueiras et al., 2019). To date, no attempt has been made to leverage satellite imagery to estimate the crop phenology in East African smallholder systems.

Despite an extensive global body of research on crop phenology and land use/land cover (LULC) classification, such information is still scarce in Africa (Adole et al., 2016; Bégué et al., 2020; Hannerz and Lotsch 2008). In Uganda, where agricultural land accounts for 72% of the total available land area, the vast majority is cultivated by smallholder farmers (Aguilar et al., 2018; The World Bank 2020), for whom food security is a major challenge that is projected to worsen under changing climatic patterns and population increase (Khan et al., 2014). The derivation of reliable agricultural estimates remains an immensely relevant topic and a particularly complicated one for smallholder farming systems due to their heterogeneous environment. Irregular field boundaries, fields too small for satellite analysis, frequent presence of trees in fields and inter- or mixed cropping practices heavily contribute poor results of estimations in the East African agricultural context, even when methodologies were successfully implemented elsewhere (Crespin-Boucaud et al., 2020; Kpienbaareh et al., 2021).

This research is aimed at building on existing knowledge of sensor harmonization to improve temporal coverage, cloud computing to allow for processing of large data sets and crop phenology to effectively monitor the growing seasons, and by doing so adapting the findings for a case study in Uganda. We specifically aim to: (i) derive a thematic LULC map for the study area based on comprehensive in situ crop data, (ii) extract the phenological metrics over one season from the harmonized Landsat sensors and Sentinel-2 product using localized land use information, (iii) examine phenological response patterns of smallholder farming systems by relating the phenology to specific agricultural classes and (iv) demonstrate the potential transferability of the methodology in space and time.

2. Materials and methods

2.1. Study area

The study area for this research is located in Kamuli district, in Eastern Uganda (Fig. 1). The area lies on average 1100 m above sea level in the flatlands between Lake Victoria to the South and Lake Kyoga to the North. In terms of climate, the region is part of the savanna climate zone, with the majority of rainfall (>1100 mm on average) occurring during March to May (MAM) and September to

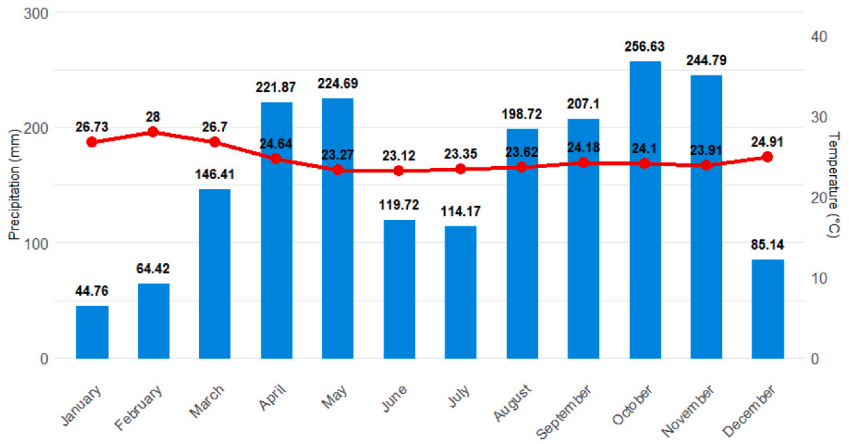

Fig. 2. Monthly average temperature and precipitation measured in Kamuli town at an elevation of 1095 m above sea level. Data source: (Weather and Climate 2023).

December (SOD) months. The remaining months experience less than 60 mm of rainfall on average (Beck et al., 2018) (Fig. 2). This results in a bimodal growing season pattern with two growing seasons from March to June and September to December. The population of the district mostly performs small-scale farming, animal grazing and fishing. The local farmers cultivate a wide variety of staple and cash crops, most noteworthy are maize, sugarcane, legumes, bananas, and coffee.

2.2. Data

2.2.1. Satellite data for LULC classification

10–20 m Sentinel-2 and Sentinel-1 imagery spanning the period from January 01, 2022 to September 01, 2022 were used for land use/land cover mapping of the area. Based on cloud cover, a total of 17 optical and radar image pairs were selected. Each image pair contained Sentinel-2 and Sentinel-1 images acquired within 5 days of each other.

2.2.2. Satellite data for sensor harmonization

With the aim of obtaining a dense cloud-free and cloud shadow-free time series spanning the whole year of 2022, several steps were performed to prepare the imagery. The image collections of Landsat 7 Enhanced Thematic Mapper Plus (ETM+), Landsat 8 and 9 Operational Land Imager (OLI), and Sentinel-2 Multispectral Instrument (MSI) were filtered for our study area and the study duration using general spatial and temporal filtering methods in Google Earth Engine (GEE) (Gorelick et al., 2017). Top-of-Atmosphere (TOA) collections were selected, and Sensor Invariant Atmospheric Correction (SIAC) was applied (Yin et al., 2022). Utilizing the same atmospheric correction method on imagery from different sensors allowed us to minimize the discrepancies in atmospheric effects exerted on the satellite imagery. Cloud and cloud shadow masking was then executed. Quality Assessment (QA) bands generated from the CFMASK algorithm (Zhu et al., 2015; Qiu et al., 2019) were used to remove pixels containing cloud contamination in the Landsat sensors. Cloudy pixels in Sentinel-2 were masked using the cloud probability band with the probability value set to less than 25 % (Zupanc 2017). Pre-processing was concluded by addressing the different solar and view angles associated with satellite sensors, by applying a Bi-directional Reflectance Distribution Function (BRDF) correction (Roy et al. 2016, 2017; Claverie et al., 2018). This allowed us to adjust the viewing and illumination angles of the satellite imagery. The BRDF correction was applied in the GEE cloud computing environment (Poortinga et al., 2019; Nguyen et al., 2020).

2.2.3. In situ data

A field campaign in the study area took place in July of 2022. During this time, the growing season was in its peak vegetative state which allowed us to accurately gather the most prominent land cover and crop types in the area. Corner and center coordinates of each agricultural field were captured using GPS Coordinates App Version 4.71 (174). Afterwards the data points were imported to the QGIS version 3.22.6 and overlayed on a satellite basemap for small border adjustments. The Minimum Mapping Unit (MMU) for reference data was set to 10 x 10 m. Built-up and water classes were added post data gathering using satellite basemap layer. The distribution of the LULC classes in terms of the number of reference points and smallest polygon size can be seen in Table 1. The data gathering campaign concluded with farmer interviews to get a better understanding of the agricultural tendencies in the area as well as farmers perspective on the state of the local climate and its impact on farming.

2.2.4. National meteorological and agricultural data

Seasonal rainfall performance data used in this study was gathered from the reports published by the Uganda National Meteorological Authority (UNMA). The inputs for this data are drawn from a variety of sources including the World Meteorological

Table 1
Distribution of land use/land cover classes in terms of number of pixels, n = 10 x 10 m. The smallest polygon size per class, user and producer accuracies together with F1 scores expressed for each class in the classification. The classes are ranked in descending order by User Accuracy.

Class types	Number of points (n)	Smallest polygon (m^2)	User Accuracy (UA) %	Producer Accuracy (PA) %	F1 Score
Water	15673	40063.6	100.00	100.00	1.00
Cotton	1503	695.9	100.00	100.00	1.00
Bare soil	26419	468.4	100.00	71.55	0.83
Maize and coffee	2938	112.4	100.00	70.00	0.82
Cassava	139	110.6	100.00	61.11	0.76
Banana	152	247.0	97.37	74.75	0.85
Coffee	1071	102.8	95.73	72.26	0.82
Shrubland	2246	171.7	94.52	71.88	0.82
Banana and coffee	1142	113.7	94.74	74.23	0.83
Sweet potato	7994	104.4	92.96	66.67	0.78
Sugarcane	13209	415.9	92.09	78.17	0.85
Grassland	1663	121.4	91.08	95.26	0.93
Rice	98	102.5	90.63	98.07	0.94
Forest	896	409.7	88.30	99.28	0.93
Maize and cassava	231	112.9	85.71	54.55	0.67
Maize and beans	1979	101.2	85.66	73.77	0.79
Maize and groundnuts	8668	114.6	85.48	80.30	0.83
Built-up	12245	1852.7	84.18	99.88	0.91
Maize	2000	109.0	77.89	93.55	0.85
Flooded vegetation	6234	461.2	69.00	94.15	0.80

Organization's Global Producing Centers (WMO GPC). Probabilistic and deterministic models were used together with local expert interpretation to derive the seasonal rainfall performance and outlooks for each growing season (Elweru, 2022; Mugume, 2022). The outputs consist of monthly rainfall estimates in millimeters on district level and qualitative comparisons against the Long-Term Mean (1991–2020). Additionally, seasonal agricultural performance from the Global Information and Early Warning System (GIEWS) unit of the Food and Agriculture Organization of the United Nations was used as a reference to our findings (FAO, 2022b).

2.3. Methods

The methodological workflow consisted of four components (Fig. 3): (1) preprocessing of satellite imagery for LULC classification; (2) LULC classification; (3) sensor harmonization; and (4) phenological metrics extraction. The first part followed a common pre-processing framework used in preparing the optical and radar satellite data for LULC classification. The second segment used the output of the first part to train the classification model and to derive the thematic map of the study area. In the third section, Landsat sensor data was adjusted and calibrated against Sentinel-2 to produce a harmonized image stack. The image stack was then used to generate a dense NDVI time series. In the last part, the LULC classification output of parts 2 and the dense NDVI time series of part 3 were combined to generate phenological metrics for each agricultural class during the first growing season of 2022.

2.3.1. Preprocessing of satellite imagery for LULC classification

Sentinel-2 Level 2 data comes in Surface Reflectance (SR) values which have been atmospherically, terrain and cirrus corrected using the sen2cor processer developed by the European Space Agency ESA (Main-Knorn et al., 2017). Clouds and cloud shadows were removed from Sentinel-2 imagery using the QA60 cloud mask and the Sentinel-2 cloud mask probability (Zupanc 2017). A quality mosaic was then created based on the maximum NDVI value on a per-pixel basis. Several spectral indices were created to further improve the classification effort. These include Enhanced Vegetation Index (EVI), Soil Adjusted Vegetation Index (SAVI), Normalized Difference Vegetation Index (NDVI), Green Normalized Difference Vegetation Index (GNDVI) and Normalized Difference Moisture Index (NDMI).

The pre-processing of Sentinel-1 Synthetic Aperture Radar (SAR) data began with updating the orbit information. After applying the most recent orbit file, we used thermal noise removal to address the background energy generated by the receiver. The background energy tends to increase the radar reflectivity values which results in less precise reflectivity estimates. Original Sentinel-1 Level 1 data contains notable radiometric bias (Miranda and Meadows 2012). To address this, we applied radiometric calibration. Radiometric calibration is an essential step in making SAR data comparable with other sensor data. The resulting SAR data contains pixel values which more accurately depict radar backscatter of the measured surfaces. Speckle filtering is subsequently applied to minimize the salt and pepper effect inherent in SAR imagery. For the speckle filtering, we used the Lee Sigma filter method. In order to minimize the distortions caused by topographic variations in an image scene, terrain correction is applied. In doing so, the image scenes were corrected for topographic distortions and afterwards reprojected to geographic projection. All pre-processing steps were executed in the Sentinel Application Platform (SNAP) toolbox version 9.0 developed by the ESA. Lastly, the Sentinel-1 scenes are subset to the study area and the Radar Vegetation Index (RVI) is calculated. Sentinel-1 and Sentinel-2 images were then stacked and projected to a common map projection.

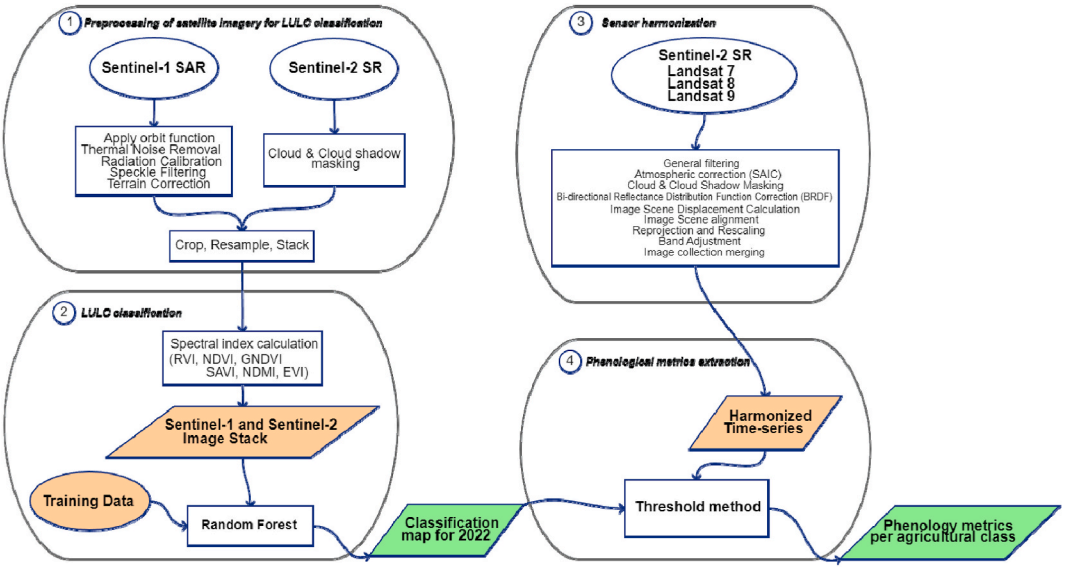

Fig. 3. The theoretical structure of the study is divided into four sections: Part 1 is centered around the preprocessing of the Sentinel-1 SAR and Sentinel-2 optical data for classification purposes; Part 2 utilizes the pre-processed imagery from Part 1 and field data to generate a thematic map of the area; Part 3 corrects the Landsat imagery and fuses it with the Sentinel-2 image collection to form a harmonized time-series; Part 4 combines the inputs from Parts 3 and 4 to extract the phenological metrics of the agricultural classes in the area.

2.3.2. LULC classification

A machine learning approach was selected for the purpose of land use/land cover classification. We used supervised Random Forest (RF) (Breiman 2001), a well-known algorithm which has been successfully used in several similar classification efforts (Crespin-Boucaud et al., 2020; Kpienbaareh et al., 2021). An important feature of RF is that each decision tree is generated by a random selection of training data and features. Majority voting of the decision trees is used to determine the classification outcome. The key user-defined features for this algorithm are the number of decision trees (ntree) and the number of variables to be used for decision tree building (mtry). Parameter tuning was applied to determine the optimal values of mtry and ntree using the tuneRF(.) function in the R-package caret (Kuhn 2008). These values were set to 500 decision trees (ntree) and the split value (mtry) of the square root of the total number of features which are the standard default settings (Breiman 2001). Subsequently, different training data split ratios were tested to find an optimal training-validation split ratio. The training data was split, with 70 % of data used for training and the remaining 30 % used for validation. Stratified sampling was used in order to prevent the disproportional representation of classes during data splitting. K-fold cross validation was applied with the number of folds set to 5. The performance of the classification was assessed visually using local knowledge and statistically through a confusion matrix, Cohen's kappa value as well as user and producer accuracies (Congalton 1991). The classification was performed in RStudio version 4.1.2 using the randomForest(.) package (Liaw and Wiener 2002). Finally, a mask layer was derived containing the land use class, which included the following classes of monocultures: sweet potato, rice, cassava, banana, cotton, coffee, maize and sugarcane; as well as the following intercrops: maize and groundnuts, banana and coffee, maize and cassava, maize and coffee, maize and beans.

2.3.3. Sensor harmonization

The alignment between the Landsat and Sentinel-2 images was improved by measuring the image scene displacement and adjusting accordingly (Storey et al., 2016). This was achieved by calculating the spatial displacement between a Sentinel-2 image and an overlapping Landsat image using the displacement(.) function in GEE and subsequently aligning the two images using the displace(.) function (GEE 2023). Next, the images were reprojected to EPSG:32658 – WGS 84 map projection and rescaled to Sentinel-2 native spatial resolution of 10 × 10 m by using a bilinear resampling method. The adjustment of spectral bands followed. Different coefficients from the literature (Flood 2017; Claverie et al., 2018; Chastain et al., 2019) were examined for Landsat 7 and Landsat 8. In the methodologies where site-specific band adjustment coefficients are presented, these results are tested for our area of interest. Correlation coefficients from Chastain et al. (2019) and Flood (2017) were selected for Landsat 8 and Landsat 7, respectively. Landsat 9 is a relatively recent sensor for which literature on band adjustment coefficients was limited. Therefore, we derived our own coefficients based on 2022 satellite imagery scenes from Sentinel-2 and Landsat 9. Once the Landsat spectral bands were adjusted the sensors were merged into a single image collection. The current study made use of previously published methods on sensor harmonization, such as BRDF correction implemented in GEE by (Poortinga et al., 2019; Nguyen et al., 2020) and SIAC atmospheric correction by (Yin et al., 2022).

2.3.4. Phenological metrics extraction

A harmonic curve was fitted on the NDVI time series observations to smooth the observed data. Cubic interpolation was then applied for gap filling purposes as proposed and implemented in GEE by Descals et al. (2020). Phenological metrics were extracted by applying a variable threshold method (Vrieling et al., 2013; Liu 2019; Bolton et al., 2020; Descals et al., 2020; Descals et al., 2021). The NDVI ratio was used for setting the threshold (White et al., 1997). The ratio was calculated using the absolute maximum and minimum values of the NDVI during the first growing season. The start of season (SoS) and end of season (EoS) are denoted as the first and last days when the NDVI time series of a pixel exceeds the local 50 %-threshold (White et al., 2009). The duration of season is calculated by subtracting the date of EoS by the date of SoS. Likewise, the maximum NDVI value is calculated between the SoS and EoS. The phenological extraction was applied on a pixel-by-pixel basis for each land use class derived from the before-mentioned LULC classification.

2.3.5. Validation of the harmonized Landsat NDVI product for 2022

The study used statistical analysis presented and implemented in Filgueiras et al. (2019) to evaluate the harmonization efforts. Agricultural fields recorded during the field campaign (see 2.3.2) were used as sample locations. Harmonization performance was assessed based on 1600 NDVI measurements for each sensor pair. The difference between the modelled Landsat NDVI values and the reference Sentinel-2 NDVI values were measured by calculating the mean-absolute deviation (MAD) (Equation (1)). The correlation between the NDVI products was examined by calculating the Pearson correlation coefficient, r (Equation (2)). The correlation coefficient ranges between −1 (indicating a strong negative relationship between two variables) and +1 (indicating a strong positive relationship between two variables). The statistical significance was determined by the probability value, p-value, which was determined using the t-distribution table for the degrees of freedom, df set to n-2, where n is the number of NDVI values. The p-value determines the acceptance or rejection of the null hypothesis, H_0, which states that there is no significant correlation between Sentinel-2 NDVI (the independent variable) and Landsat harmonized NDVI (the dependent variable). The significance level, alpha (α), was set to the standard value of 0.05. A p-value lower than 0.05 will imply rejection of the null hypothesis and conclude that the relationship between Sentinel-2 and Landsat NDVI values is significant.

$$MAD = \frac{\sum_{i=1}^{n} |y_i - \hat{y}_i|}{n} \quad (1)$$

Where the number of samples is denoted as n, y_i is the actual value and $\hat{y}_i$ is the predicted value.

$$r = \frac{\sum (x - m_x)(y - m_y)}{\sqrt{\sum (x - m_x)^2 + \sum (y - m_y)^2}} \quad (2)$$

Where m_X and m_Y correspond to the means of the two groups and n is the sample size.

Boxplots showing the absolute NDVI anomalies and day differences between Sentinel-2 and Landsat sensors were generated to reveal how the harmonized NDVI values of Landsat behave in comparison to Sentinel-2 NDVI values with varying days between them. Using the same principle, the scatterplots between the absolute NDVI anomalies and time of the year were generated as well. These plots were used to compare the harmonization performance during the growing season and during the offseason, as well as between different number of days in between Sentinel-2 and Landsat images.

3. Results

3.1. Accuracy assessment of the LULC classification using SAR data from Sentinel-1 together with the optical data from Sentinel-2

An example on of the thematic LULC classification map is shown in Fig. 4. The overall accuracy (OA) of the random forest classification was 87.9 % with Cohen's kappa value of 0.83. Well-defined classes such as water and bare soil yielded highest accuracies throughout the study area with user accuracy equaling 100 % (Table 1). Some agricultural classes also recorded high accuracies, most notably cotton, maize and coffee, cassava and banana. For these agricultural classes the user accuracies remained above 95 % with varying producer accuracies. The majority of maize intercropping systems showed lower accuracies. Nevertheless, the user and producer accuracies show good overall performance in discriminating the most common staple crops (Table 1). The class-by-class accuracy matrix reveals a moderate degree of misclassification occurring among the maize-dominated classes. Another source of error in classification arose from the sugarcane class, with several data samples from other classes being incorrectly classified as sugarcane. Flooded vegetation appears to be the class with the most misclassified pixels.

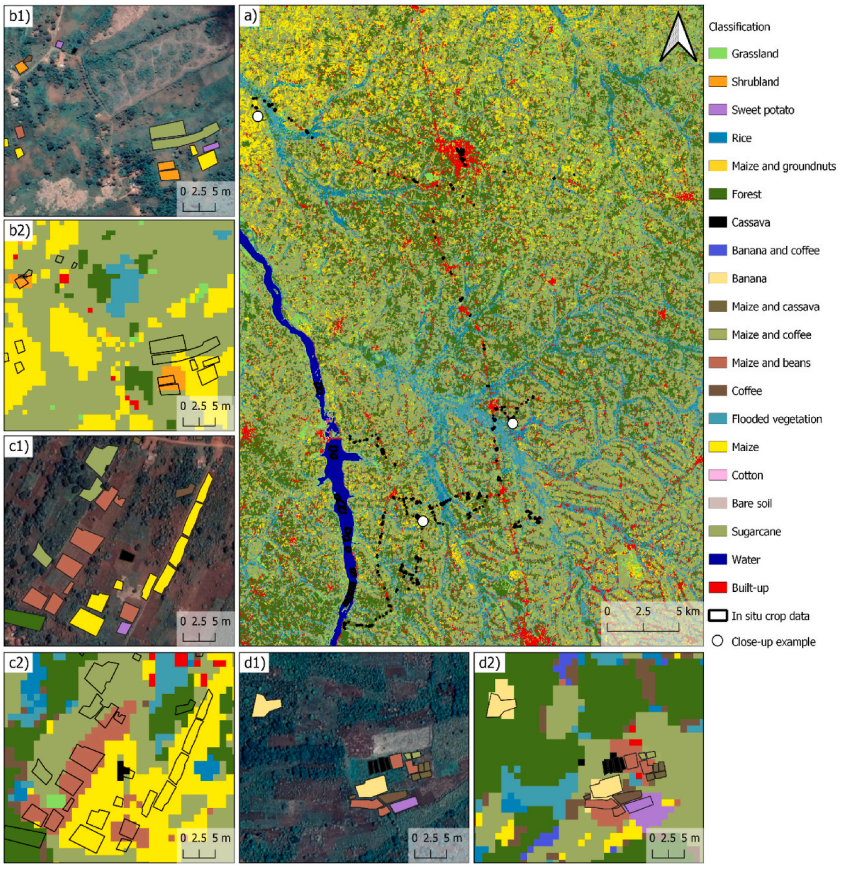

Fig. 4. Classification map of the study area a) with a close-up of sites b), c), d) showing the training data overlayed on Google Earth satellite layer b1), c1), d1) and the resulting LULC classification map of the close-up area b2), c2), d2).

3.2. Performance of harmonized Landsat NDVI timeseries

The comparison between synthetic NDVI values of Landsat data and Sentinel-2 NDVI values are shown in Fig. 5. Band adjustment coefficients created for Landsat 9 can be found in the appendix. Among the Landsat harmonized products, Landsat 9 showed the highest correlation with Sentinel-2 ($R^2 = 0.59$). Landsat 7 and Landsat 8 recorded good relation as well with Squared Pearson coefficients of 0.44 and 0.45 respectively. The performed correlation analysis reveals a significant association between all Landsat products and the reference Sentinel-2, i.e. p-value <0.005. The highest correlation between Landsat 9 and Sentinel-2 is supported by the MAD value of 0.0522. Landsat 8 and Landsat 7 harmonized NDVI product registered similar MAD values of 0.0522 and 0.0566.

Further, the results indicate no significant decline in harmonization performance with an increase in days between Sentinel-2 and Landsat acquisitions (Fig. 6). This implies that a period of five days is not long enough for the vegetation to change significantly, from a remote sensing point of view. The interquartile range (IQR) for all three sensor pairings does not exceed an absolute NDVI difference of 0.1 indicating that the majority of synthetic NDVI values differs slightly from the referenced NDVI values. This is true regardless of the day-difference between Sentinel-2 and all three Landsat sensors with a single exception being the one-day difference between Sentinel-2 and Landsat 7 (Fig. 6a). The analysis of Landsat 7 and Landsat 9 harmonized products show an increase of potential outliers between days one and four (Fig. 6a and c). This does not hold true in instances when the images overlap (i.e. same day images) or when they are five days apart. Sentinel-2 and Landsat 8 pair features potential outliers on all overlapping distances except when images are four days apart. The highest number of potential outliers are observed when images have no overlap or are five days apart.

As expected, the harmonization performance was generally better during the growing season in comparison to the off-season, since the NDVI is maximized in this period (Fig. 7). The MAD values are higher for all Landsat products during the growing season, indicating the better model fit and smaller deviation between synthetic and referenced NDVI values during this period. The discrepancy of the model performance is most visible in the case of Landsat 9. Here the mean-absolute deviation during the growing season is much greater at 0.0459 as compared to the offseason value of 0.0596 and the correlation coefficient during the growing season is much higher at 0.71 compared with 0.48 during the offseason. Other Landsat products display a slight improvement during the growing

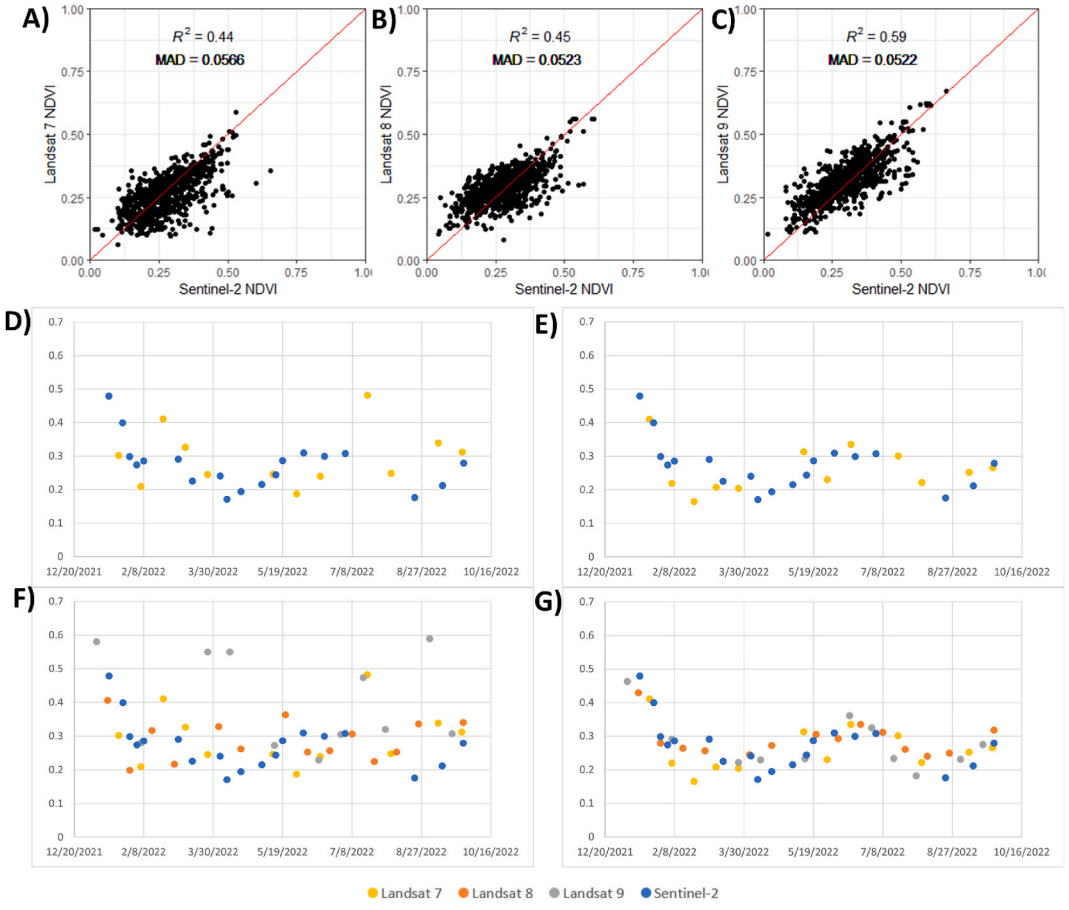

Fig. 5. The scatter plots (A – Landsat 7, B – Landsat 8, C – Landsat 9) compare the NDVI values of Sentinel-2 (reference NDVI) with harmonized Landsat NDVI values (synthetic NDVI) based on 1600 NDVI measurements for each sensor pair. Every plot features a solid red line (1:1) that is used to visualize the correlation between reference and synthetic NDVI values. Temporal NDVI time series of Sentinel-2 and Landsat 7 are shown before and after harmonization (D and E). NDVI time series over a crop pixel in the study area before and after harmonization for all sensors is shown in F) and G) respectively. (For interpretation of the references to color in this figure legend, the reader is referred to the Web version of this article.)

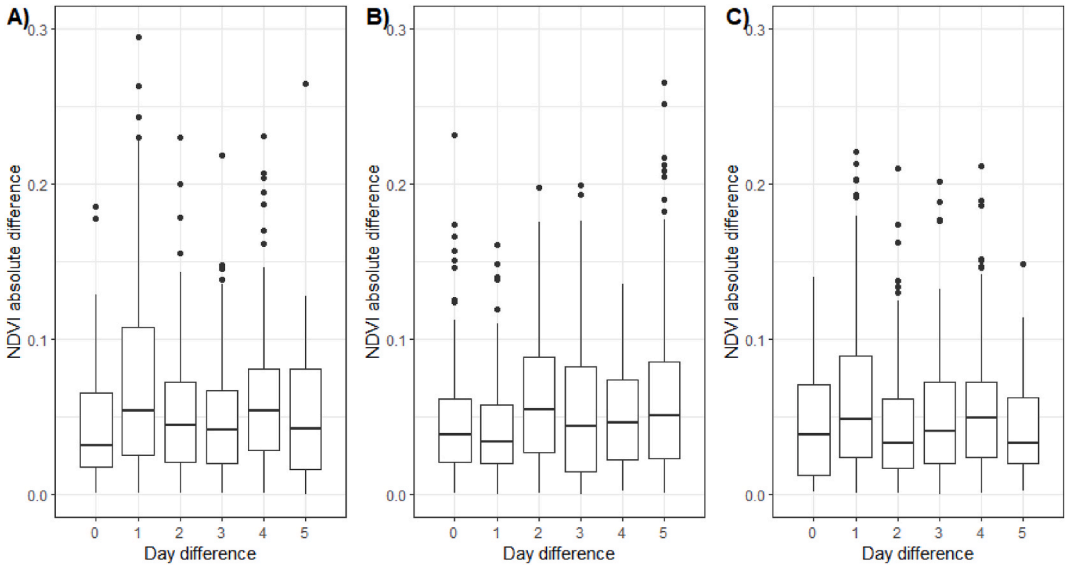

Fig. 6. The boxplots compare the NDVI deviation between Sentinel-2 and Landsat sensors (A – Landsat 7, B – Landsat 8, C – Landsat 9) as a function of days separating the paired Sentinel-2 and Landsat image scenes.

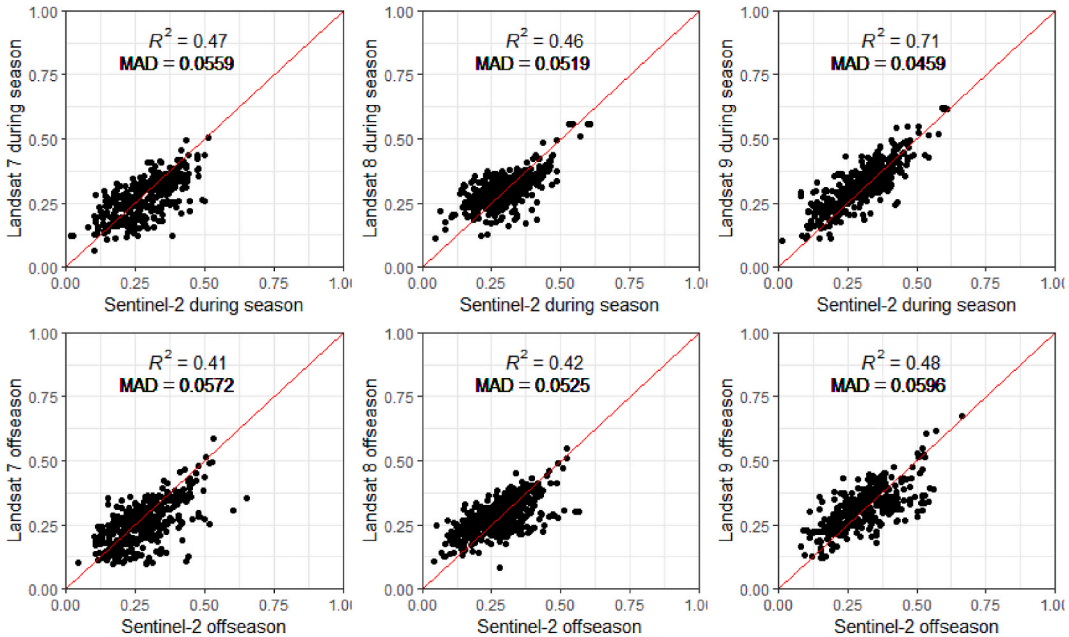

Fig. 7. The scatter plots show the NDVI anomalies between Sentinel-2 and Landsat sensors based on the time of the year. During season is associated with rainy seasons occurring in periods March to May (MAM) and September to December (SOD) while offseason is associated with the remaining months. Every plot features a solid red line (1:1) that is used to visualize the correlation between reference and synthetic NDVI values. (For interpretation of the references to color in this figure legend, the reader is referred to the Web version of this article.)

season.

3.3. NDVI profiles of the dominant land use types in the study area

The NDVI time-series signatures (Fig. 8) represent the average vegetation pattern for each agricultural class in the area of interest. The majority of crops show a clear onset and end of the growing season. This is especially clear for maize-dominated classes such as maize, maize intercropped with beans, and maize intercropped with groundnuts. The end of the growing season for these crops as well as for sweet potato and cassava usually signifies a full clearance of the agricultural field by means of harvest. In other classes (i.e. banana, sugarcane, coffee, etc.) the harvest of the yield is not equal to a full removal of the plants in the field. This may result in less

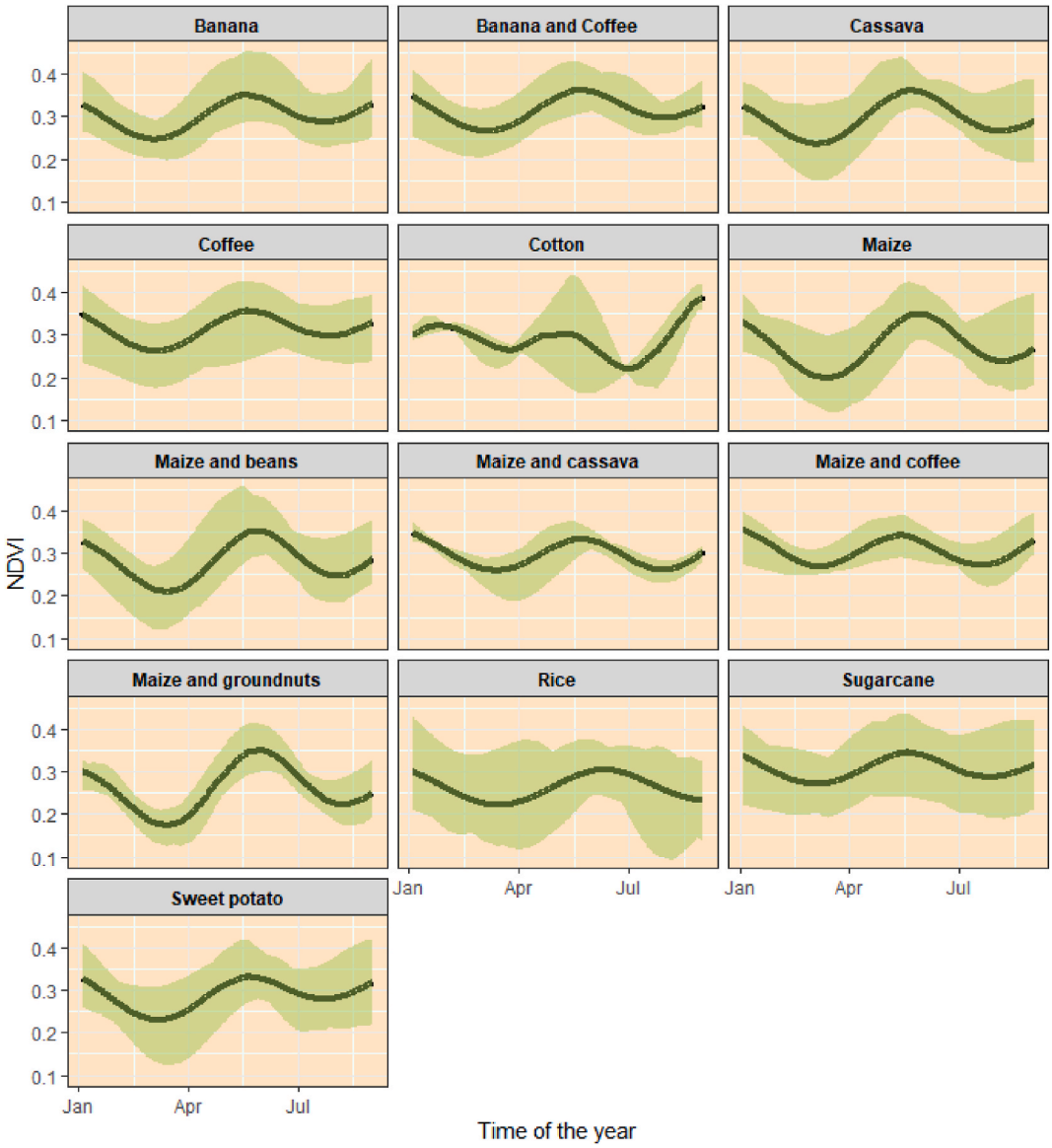

Fig. 8. NDVI profiles of the most prominent crop and intercropping types in the study area. The dark green NDVI signatures are modelled and averaged for each class while light green shows the upper and lower values. (For interpretation of the references to color in this figure legend, the reader is referred to the Web version of this article.)

profound declines in NDVI signatures during the end stages of the season, as can be seen in banana, sugarcane and coffee classes. For all agricultural classes, low NDVI values have been recorded for the growing season in focus.

Cotton, maize intercropped with coffee and sugarcane have the earliest onsets of the growing season with an average onset occurring on the 81st Julian calendar day (JCD) for Cotton and 86th JCD for both sugarcane and maize with coffee (Table 2). This equates to 22nd and 27th of March respectively. The other maize classes appear to have the latest onsets with maize and groundnuts, maize and beans, and maize monocrop all beginning in mid to end of April. The end of the growing seasons appears to be more uniform, with the majority of cropping seasons terminating within a two-week period between the 170th and 184th Julian calendar day (19th of June and 3rd of July respectively). Two exceptions here are the Cotton and Maize with coffee classes which end earlier on the 20th of May and 13th of June respectively.

The maximum vegetation of each crop, measured by the maximum NDVI value show that the majority of agricultural classes fall within the range of 0.4–0.5, with the exception of cassava which shows a higher NDVI value of 0.55. Fields containing maize-dominated agriculture display a fairly similar maximum NDVI signature, with maize monocrop and maize and beans having the higher NDVI values. The smallest value is registered by maize and cassava albeit by a small margin. Overall, the NDVI values are quite low for agricultural areas, which can be an indicator of unfavorable weather conditions during this growing season.

Table 2
Phenological metrics per agricultural class. Start of Season is denoted as SoS, End of Season is denoted as EoS and maximum NDVI as maxNDVI. The duration of the season is expressed in the amount of days between EoS and SoS.

Class	mean SoS (JCD)	mean EoS (JCD)	Duration (Days)	maxNDVI
Banana	89	176	87	0.47
Banana and coffee	97	170	74	0.49
Cassava	100	185	85	0.55
Coffee	93	183	90	0.48
Cotton	81	140	58	0.46
Maize	108	182	74	0.49
Maize and beans	110	182	72	0.50
Maize and cassava	99	182	83	0.44
Maize and coffee	86	164	78	0.45
Maize and groundnuts	112	186	74	0.46
Rice	103	192	89	0.49
Sugarcane	86	173	87	0.46
Sweet potato	99	181	83	0.48

The duration of growing seasons for each agricultural class reveals a high variance between classes. Cotton ranks lowest, with an average seasonal duration of 58 days, followed by maize and beans (72 days), maize and groundnuts (74 days) and maize. All maize-dominated classes show an average duration of the season of approximately two and a half months. Coffee, rice, sugarcane and banana rank on the higher end of the chart. Their seasonal durations are 90, 89, 87 and 87 days respectively. Overall, between the agricultural class having the shortest duration (cotton) and the one having the longest duration (coffee) there is a 32-day difference which indicates a considerable discrepancy between agricultural classes in the area.

3.4. Extraction of phenological metrics in the study area

The phenological analysis of agriculture in the entire study area can be seen in Fig. 9. The southern part of the area overall exhibits an earlier onset of the growing season, with high variation in the onset of the season seen from the contrasting colors. Here the onset of the growing season started from early March to late June. The northern part seems to have a later onset of the season, with the soft green color indicating the onset occurring approximately in late March – beginning of April in the majority of the fields.

3.5. Comparison of seasonal phenological metrics with UNMA seasonal climatological reports and agricultural assessment reports of GIEWS

Based on the GIEWS report on the regional agricultural performance for the first growing season in Uganda, the harvesting of the major staple crops was completed in August which results in an approximate delay of one month. This delay is attributed to severe deficit and a late onset of March–June rainfall (Elweru, 2022; FAO, 2022b). The rainfall deficit contributed to a decreased agricultural output that led to a third consecutive season with below average yield (FAO, 2022b). The decreased crop production reported in (FAO, 2022b) has been reflected in our low overall NDVI values for all staple crops (Fig. 8). All crop types analyzed in this study had growing season onsets in the end of March and beginning of April which coincides with the seasonal performance documented in climatological

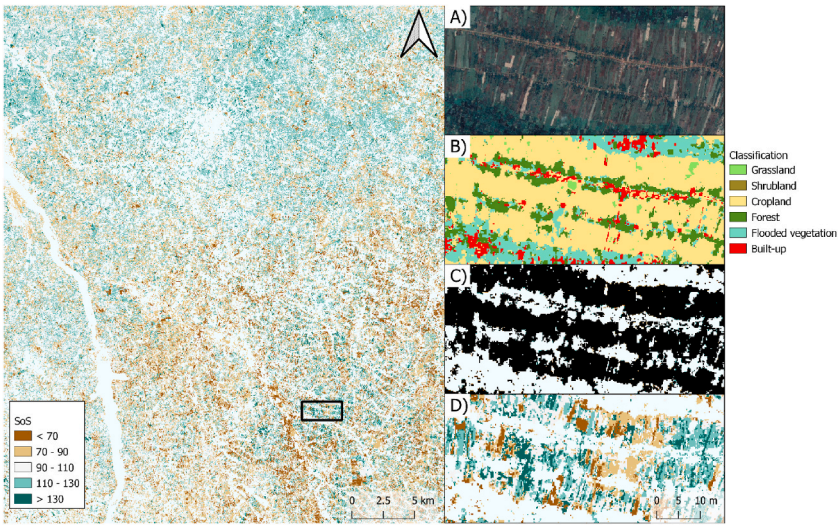

Fig. 9. Start of the long growing season in the spring of 2022 for the agricultural class in the study area. Subplot A) shows the satellite imagery layer for the selected example area as true color composite, subplot B) shows the thematic classification of the area; C) shows the cropland mask where cropland is displayed in black and non-cropland pixels displayed in white color, and D) shows the start of the growing season for the applied area. (For interpretation of the references to color in this figure legend, the reader is referred to the Web version of this article.)

reports of UNMA and agricultural assessment report of GIEWS.

4. Discussion

The phenological patterns of diverse, small-scale cropping systems can be captured by harmonization of multiple sensors combined with a large set of in-situ data. Previously unavailable Landsat 9 band adjustment coefficients were derived allowing us to integrate Landsat 9 images into our methodology. The harmonization of Landsat and Sentinel-2 resulted in a cloud-free image every three to four days providing us with the necessary temporal coverage of smallholder fields. The combination of the novel, high resolution LULC map derived from Sentinel-1, Sentinel-2 and in situ data with harmonized NDVI time-series allowed us to examine the phenological patterns of 13 crop types in the study area, signifying the first field-level phenological metrics estimation bi-modal settings at spatially explicit resolutions.

4.1. LULC classification performance

The classification yielded satisfactory results (OA = 87.9 %, Cohen's kappa = 0.83) which allowed us to effectively discriminate between the most prominent land use/land cover classes in the area and in doing so to produce an up-to-date thematic map previously unavailable in the research area. The RF classifier faced notable issues discriminating between intercropping classes. This was to be expected since many training data fields contain a similar primary crop, namely maize. Most notably maize-dominated classes intercropped with groundnuts, and cassava had user accuracies of 85 %. Another anomaly was caused by the Sugarcane class. During the time of the image acquisition and field campaign, the farmers within the study area benefited from high refined sugar prices. This forced many smallholder farmers to switch cultivation to sugarcane. Because of its high stalks and long thin leaves, sugarcane might often be misinterpreted as flooded vegetation, shrubland or grassland. In addition, the faster maturation of the plant allows it to be harvested quicker than most staple crops. This can lead to some fields already being harvested, while others are still growing during satellite image acquisition. This results in the sugarcane class having a broad spectral and textural profile, which makes it difficult for a classifier to correctly assign the appropriate class. These dynamics illustrate the difficulty of mapping intercropping systems which was reported in previous cropping system identification studies as well (Ibrahim et al., 2021; Kpienbaareh et al., 2021). Ibrahim et al. (2021) reported an overall accuracy of 84 % when using Sentinel-2 and SkySat data in mapping intercropping systems of Nigeria. An overall accuracy of 85.8 % and Cohen's kappa coefficient of 0.83 were recorded in Malawi where random forest algorithm was applied on Sentinel-1, Sentinel-2 and PlanetScope imagery. This indicates that the quality of our classification is in line with similar crop type mapping studies throughout Africa.

4.2. Harmonization performance

We derived our own Landsat 9 adjustment coefficients based on 2022 satellite imagery from Sentinel-2 and Landsat 9 due to the recent nature of Landsat 9 data and lack of literature on band adjustment coefficients. The harmonized Landsat products correlated well with the Sentinel-2 data. Landsat 9 and Landsat 8 synthetic NDVI values showed the highest accuracies with the MAD values of 0.0522 and 0.0523 respectively. In theory, better performance of Landsat 8 and 9 over Landsat 7 is to be expected, as both sensors share the same spectral bandwidths which also have a greater spectral overlap with Sentinel-2 bands in comparison with Landsat 7. The improved correlation as a result of greater spectral band overlap was observed in a previous publication as well (Chastain et al., 2019).

The harmonization of Landsat products was generally better during the growing season when compared with the off-season (Fig. 7). The Landsat 9 harmonized product shows a clear improvement during the growing season with an average increase in accuracy of 0.0137. Landsat 7 and Landsat 8 have both showed improvements as well, albeit by small margins of 0.0013 and 0.006 respectively. Higher vegetation cover during the growing seasons seemed to lead to better harmonization between sensors which is supported by earlier findings by (Xu and Guo 2014).

While the native geometric resolution of the Landsat sensors is 30-m, the complex nature of agricultural fields and their small sizes in the Kamuli district of Uganda make it difficult to contain pure agricultural pixels without including nearby objects (i.e. trees, houses, roads, etc.). The harmonization performance was analyzed on 10-m resolution by resampling the Landsat images in GEE. The rescaling did not inquire a significant loss of data quality. The combined use of Landsat and Sentinel-2 provided a cloud-free image for each pixel every three to four days. The sole use of the Sentinel-2 constellation would provide a revisit time of five days prior to cloud and cloud shadow masking. Thus, inclusion of the Landsat sensors greatly increases the temporal coverage of the target areas and reduced the need for interpolation.

4.3. Seasonal phenology prediction validation

The estimated start and end of the growing seasons were compared with the meteorological data by examining the rainfall outlooks and seasonal predictions by UNMA and GIEWS. The rainfall for March of 2022 was characterized by dry spells over majority of Uganda, including the Kamuli district (Elweru, 2022). The start of seasonal rains was disturbed by a sequence of Tropical Cyclone developments in the Indian Ocean resulting in moist air being diverted from East Africa to the Madagascar area (EUMETSAT 2023). This resulted in below-normal rainfall activity in March and beginning of April. The rainfall stabilized in the second part of April and normal conditions proceeded the rest of the long growing season of 2022 in the Kamuli district. Delayed onsets of rainfall leads to delayed vegetation development (Gordo and Sanz 2010). This rainfall shortage in March and ensuing delayed onset of the growing season was reflected in our seasonal estimates as all crop types had growing season onsets at the end of March and beginning of April. Moreover, the below-average maximum NDVI values captured in our study (Fig. 8) corresponds well with the climatological data and reflect the

theoretical response between climatic variables and phenology.

In addition, the LULC map introduced in the earlier section, classified substantial areas in the southern part of the study area as flooded vegetation (Fig. 4). The presence of flooded vegetation implies higher accessibility of water for agricultural purposes and higher water content in the soil. This could be one of the reasons explaining why the southern part of the area was less susceptible to the delayed rainfall and subsequent delayed onset of the growing season shown in Fig. 9.

The large amounts of sugarcane present another possible explanation for very high variance in growing season onsets in the study area. Sugarcane is a perennial crop which, unlike other annual crops, does not need to be replanted every growing season. The usual planting time of sugarcane is at the start of the rainy season, however planting in the middle of the rainy season is not uncommon as well (FAO, 2022a). Once planted, the first harvest takes place after 15–24 months depending on the region and climate conditions (FAO, 2022a). After the harvest of sugarcane, the root stalks remain intact to re-sprout and grow for another season. Because of these factors, sugarcane is less governed by the onset of the rainy season and more by the growth stage of previous crop on the field. The northern part of the study area contains large amounts of maize monocrop fields, while the southern part is largely dominated by sugarcane (Fig. 4). Fig. 9 reveals regional differences in onset of the growing seasons, with the northern parts of the study area having later onsets of the season and southern section characterized by high variance and generally earlier onsets. This indicates that the starting dates are not only area-related, but also related to the crop type.

5. Conclusions

Our research investigated the crop-specific phenological patterns for the Kamuli district, Uganda. In doing so, we demonstrated the potential of harmonized NDVI time-series from Landsat and Sentinel-2 for detecting the phenological patterns of complex smallholder agricultural systems in East Africa. We produced a novel, high-resolution LULC map for the area of interest which was not previously available. With an overall accuracy of 87.9% and Cohen's kappa value of 0.83, the classification map allowed us to effectively discriminate between the most prominent crop types. Based on the generated LULC map, we extracted the phenological metrics of the crop types using a dense, harmonized NDVI time-series and applying a thresholding method. Band adjustment coefficients for Landsat 9 were created enabling inclusion of Landsat 9 imagery in this study. Growing season phenology results show a high variance in the start of the growing season with most crop types having seasonal onsets in the end of March to mid of April period. End of growing season for the majority of crops in the area appears to be from the end of June until mid July. The maize and maize intercropped agriculture exhibit similar duration of the growing season of two and a half months while other agricultural systems have a wide range of seasonal durations from 58 days (Cotton) to 90 days (Coffee). The results suggest that combining the Landsat and Sentinel-2 sensors greatly improves the temporal coverage of the target areas, by providing a cloud-free observation every 3–4 days. The methodology provides a framework for phenological metrics estimation in highly complex and fragmented agro-ecological landscapes in East Africa. Future emphasis should be placed on application of the threshold methodology for an entire country, analysis of past growing seasons and inclusion of more field data for referencing. Uncertainties in the future climate and projected increase in abrupt temperature and precipitation variations will affect the planting patterns, therefore effective and rapid derivation of reliable agricultural outputs will play an important role for the food security in East Africa.

Funding

This publication is supported by the Open Access Publication Fund of the University of Wuerzburg. The research is a part of the project UPSCALE funded by the European Commission's Horizon 2020 research and innovation program under grant agreement No 861998 (European Commission, 2020) (accessed on July 20, 2023).

Ethical Statement

Hereby, I Adomas Liepa consciously assure that for the manuscript *Harmonized NDVI time-series from Landsat and Sentinel-2 reveal phenological patterns of diverse, small-scale cropping systems in East Africa* the following is fulfilled.

1)This material is the authors' own original work, which has not been previously published elsewhere.
2)The paper is not currently being considered for publication elsewhere.
3)The paper reflects the authors' own research and analysis in a truthful and complete manner.
4)The paper properly credits the meaningful contributions of co-authors and co-researchers.
5)The results are appropriately placed in the context of prior and existing research.
6)All sources used are properly disclosed (correct citation). Literally copying of text must be indicated as such by using quotation marks and giving proper reference.
7)All authors have been personally and actively involved in substantial work leading to the paper, and will take public responsibility for its content.
The violation of the Ethical Statement rules may result in severe consequences.

To verify originality, your article may be checked by the originality detection software iThenticate. See also http://www.elsevier.com/editors/plagdetect.

I agree with the above statements and declare that this submission follows the policies of Remote Sensing Applications: Society and Environment as outlined in the Guide for Authors and in the Ethical Statement.

CRediT authorship contribution statement

Adomas Liepa: Conceptualization, Data curation, Formal analysis, Investigation, Methodology, Software, Visualization, Writing – original draft, Writing – review & editing, Resources. **Michael Thiel:** Conceptualization, Funding acquisition, Project administration, Resources, Supervision, Writing – review & editing. **Hannes Taubenböck:** Resources. **Ingolf Steffan-Dewenter:** Resources, Funding acquisition, Project administration. **Itohan-Osa Abu:** Resources. **Maninder Singh Dhillon:** Resources. **Insa Otte:** Resources. **Michael Hilary Otim:** Funding acquisition, Project administration, Resources. **Moses Lutaakome:** Resources. **David Meinhof:** Resources. **Emily A. Martin:** Funding acquisition, Project administration, Resources. **Tobias Ullmann:** Conceptualization, Resources, Supervision, Writing – review & editing.

Declaration of competing interest

The authors declare that they have no known competing financial interests or personal relationships that could have appeared to influence the work reported in this paper.

Data availability

Data will be made available on request.

Acknowledgments

The authors express gratitude to the U.S. Geological Survey (USGS) Earth Resources Observation and Science (EROS) Center for Landsat 7, 8 and 9 imagery; The Copernicus Sentinel-2 mission for the Sentinel-2 data; Google Earth Engine platform for its cloud-computing capabilities; the Comprehensive R Archive Network (CRAN) for LULC classification generation and plot visualization using R packages, such as raster, ggplot2, tidyverse, rgdal; and the European Commision's Horizon 2020 research and innovation program for funding via the project UPSCALE (https://upscale-h2020.eu/). Lastly, the authors would like to thank the anonymous reviewers for their constructive feedback and insightful recommendations.

Appendix A. Supplementary data

Supplementary data to this article can be found online at https://doi.org/10.1016/j.rsase.2024.101230.

AppendixBand adjustment coefficients derived for this study to express Sentinel-2 MSI reflectance as a function of Landsat 9 OLI spectral bands

Band Name	Slope	Intercept
Blue – B2	0.639903557	0.136414
Green – B3	0.773585714	0.139454
Red – B4	0.9654869	0.120147
NIR – B5	0.780133671	0.122467

Derivation of adjustment coefficients followed the methodology outlined and applied in (Flood 2017; Claverie et al., 2018; Chastain et al., 2019).

References

Adole, Tracy, Dash, Jadu, Atkinson, Peter M., 2016. A systematic review of vegetation phenology in Africa. Ecol. Inf. 34, 117–128. https://doi.org/10.1016/j.ecoinf.2016.05.004.

Aguilar, Rosa, Zurita-Milla, Raul, Izquierdo-Verdiguier, Emma, de By, A., Rolf, 2018. A cloud-based multi-temporal ensemble classifier to map smallholder farming systems. Rem. Sens. 10 (5), 729. https://doi.org/10.3390/rs10050729.

Badeck, Franz-W., Bondeau, Alberte, Böttcher, Kristin, Doktor, Daniel, Lucht, Wolfgang, Schaber, Jörg, Sitch, Stephen, 2004. Responses of spring phenology to climate change. New Phytol. 162 (2), 295–309. https://doi.org/10.1111/j.1469-8137.2004.01059.x.

Beck, Hylke E., Zimmermann, Niklaus E., McVicar, Tim R., Vergopolan, Noemi, Berg, Alexis, Wood, Eric F., 2018. Present and future Köppen-Geiger climate classification maps at 1-km resolution. Sci. Data 5, 180214. https://doi.org/10.1038/sdata.2018.214.

Bégué, Agnès, Leroux, Louise, Soumaré, Mamy, Faure, Jean-François, Diouf, Abdoul Aziz, Augusseau, Xavier, et al., 2020. Remote sensing products and services in support of agricultural public policies in Africa: overview and challenges. Front. Sustain. Food Syst. 4, 58 https://doi.org/10.3389/fsufs.2020.00058.

Bolton, Douglas K., Gray, Josh M., Melaas, Eli K., Moon, Minkyu, Eklundh, Lars, Friedl, Mark A., 2020. Continental-scale land surface phenology from harmonized Landsat 8 and Sentinel-2 imagery. Remote Sensing of Environment 240, 111685. https://doi.org/10.1016/j.rse.2020.111685.

Breiman, Leo, 2001. Machine learning, 45 (1), 5–32. https://doi.org/10.1023/A:1010933404324.

Chastain, Robert, Housman, Ian, Goldstein, Joshua, Finco, Mark, Tenneson, Karis, 2019. Empirical cross sensor comparison of Sentinel-2A and 2B MSI, Landsat-8 OLI, and Landsat-7 ETM+ top of atmosphere spectral characteristics over the conterminous United States. Remote Sensing of Environment 221, 274–285. https://doi.org/10.1016/j.rse.2018.11.012.

Chen, Liding, Huang, Zhilin, Gong, Jie, Fu, Bojie, Huang, Yilong, 2007. The effect of land cover/vegetation on soil water dynamic in the hilly area of the loess plateau, China. Catena 70 (2), 200–208. https://doi.org/10.1016/J.CATENA.2006.08.007.

Cheng, Yan, Vrieling, Anton, Fava, Francesco, Meroni, Michele, Marshall, Michael, Gachoki, Stella, 2020. Phenology of short vegetation cycles in a Kenyan rangeland from PlanetScope and Sentinel-2. Remote Sensing of Environment 248, 112004. https://doi.org/10.1016/j.rse.2020.112004.

Claverie, Martin, Ju, Junchang, Masek, Jeffrey G., Dungan, Jennifer L., Vermote, Eric F., Roger, Jean-Claude, et al., 2018. The Harmonized Landsat and Sentinel-2 surface reflectance data set. Remote Sensing of Environment 219, 145–161. https://doi.org/10.1016/j.rse.2018.09.002.

Congalton, Russell G., 1991. A review of assessing the accuracy of classifications of remotely sensed data. Remote Sensing of Environment 37 (1), 35–46. https://doi.org/10.1016/0034-4257(91)90048-B.

Crespin-Boucaud, A., Lebourgeois, V., Lo Seen, D., Castets, M., Bégué, A., 2020. Agriculturally consistent mapping of smallholder farming systems using remote sensing and spatial modelling. In: Int. Arch. Photogramm. Remote Sens. Spatial Inf. Sci. XLII-3/W11, pp. 35–42. https://doi.org/10.5194/isprs-archives-XLII-3-W11-35-2020.

Descals, Adria, Verger, Aleixandre, Yin, Gaofei, Penuelas, Josep, 2021. A threshold method for robust and fast estimation of land-surface phenology using google earth engine. In: IEEE J. Sel. Top. Appl. Earth Observations Remote Sensing, vol. 14, pp. 601–606. https://doi.org/10.1109/JSTARS.2020.3039554.

Descals, Adrià, Verger, Aleixandre, Yin, Gaofei, Peñuelas, Josep, 2020. Improved estimates of arctic land surface phenology using sentinel-2 time series. Rem. Sens. 12 (22), 3738. https://doi.org/10.3390/rs12223738.

Elweru, D.W., 2022. March to May 2022 Seasonal Rainfall Outlook over Uganda. Uganda National Meteorological Authority (UNMA). Available online at: https://www.unma.go.ug/seasonal-forecasts/. (Accessed 25 April 2023).

EUMETSAT, 2023. Monitoring tropical cyclones in the Indian Ocean - 2020-2022. Available online at: https://www.eumetsat.int/monitoring-tropical-cyclones-indian-ocean-2020-present,checkedon4/25/2023.

European Commission, 2020. Directorate-General for Research and Innovation, Horizon 2020 – European Green. Deal call, Publications Office of the European Union. https://data.europa.eu/doi/10.2777/200559.

FAO, Crop Calendar, 2022a. Information tool for crop production. Available online at: http://www.fao.org/agriculture/seed/cropcalendar/welcome.do. (Accessed 30 June 2023).

FAO, GIEWS, 2022b. Country brief - Uganda. Available online at: https://www.fao.org/giews/countrybrief/country/UGA/pdf/UGA.pdf. (Accessed 26 June 2023).

Filgueiras, Roberto, Mantovani, Everardo Chartuni, Althoff, Daniel, Filho, Fernandes, Inácio, Elpídio, Cunha, Da, França, Fernando, 2019. Crop NDVI monitoring based on Sentinel 1. Rem. Sens. 11 (12), 1441. https://doi.org/10.3390/rs11121441.

Fitchett, Jennifer M., Grab, Stefan W., Thompson, Dave I., 2015. Plant phenology and climate change. Prog. Phys. Geogr. Earth Environ. 39 (4), 460–482. https://doi.org/10.1177/0309133315578940.

Flood, Neil, 2017. Comparing sentinel-2A and Landsat 7 and 8 using surface reflectance over Australia. Rem. Sens. 9 (7), 659. https://doi.org/10.3390/rs9070659.

GEE, 2023. Registering images. Image displacement and warping an image in GEE API. Available online at: https://developers.google.com/earth-engine/guides/register. (Accessed 7 June 2023).

Gordo, Oscar, Sanz, Juan Jose, 2010. Impact of climate change on plant phenology in Mediterranean ecosystems. Global Change Biol. 16 (3), 1082–1106. https://doi.org/10.1111/j.1365-2486.2009.02084.x.

Gorelick, N., Hancher, M., Dixon, M., Ilyushchenko, S., Thau, D., Moore, R., 2017. Google earth engine: planetary-scale geospatial analysis for everyone. Remote Sensing of Environment.

Hannerz, F., Lotsch, A., 2008. Assessment of remotely sensed and statistical inventories of African agricultural fields. Int. J. Rem. Sens. 29 (13), 3787–3804. https://doi.org/10.1080/01431160801891762.

Ibrahim, Esther Shupel, Rufin, Philippe, Nill, Leon, Kamali, Bahareh, Nendel, Claas, Hostert, Patrick, 2021. Mapping crop types and cropping systems in Nigeria with sentinel-2 imagery. Rem. Sens. 13 (17), 3523. https://doi.org/10.3390/rs13173523.

Imeson, A.C., Prinsen, H.A.M., 2004. Vegetation patterns as biological indicators for identifying runoff and sediment source and sink areas for semi-arid landscapes in Spain. Agric. Ecosyst. Environ. 104 (2), 333–342. https://doi.org/10.1016/j.agee.2004.01.033.

Khan, Zeyaur R., Midega, Charles A.O., Pittchar, Jimmy O., Murage, Alice W., Birkett, Michael A., Bruce, Toby J.A., Pickett, John A., 2014. Achieving food security for one million sub-Saharan African poor through push-pull innovation by 2020. Philosophical transactions of the Royal Society of London. Series B, Biological sciences 369 (1639), 20120284. https://doi.org/10.1098/rstb.2012.0284.

Kpienbaareh, Daniel, Sun, Xiaoxuan, Wang, Jinfei, Luginaah, Isaac, Kerr, Bezner, Rachel, Esther, Lupafya, Dakishoni, Laifolo, 2021. Crop type and land cover mapping in northern Malawi using the integration of sentinel-1, sentinel-2, and PlanetScope satellite data. Rem. Sens. 13 (4), 700. https://doi.org/10.3390/rs13040700.

Kuhn, Max, 2008. Building predictive models in R using the caret package. J. Stat. Soft. 28 (5) https://doi.org/10.18637/jss.v028.i05.

Liaw, Andy, Wiener, Matthew, 2002. Classification and regression by randomForest. R. News 2 (3), 18–22.

Liu, Jianhong, 2019. A phenology-based cropping pattern (PBCP) mapping method based on remotely sensed time-series vegetation Index data. In: 2019 8th International Conference on Agro-Geoinformatics (Agro-Geoinformatics). 2019 8th International Conference on Agro-Geoinformatics (Agro-Geoinformatics). Istanbul, Turkey, 7/16/2019 - 7/19/2019. IEEE, pp. 1–5.

Main-Knorn, Magdalena, Pflug, Bringfried, Louis, Jerome, Debaecker, Vincent, Müller-Wilm, Uwe, Gascon, Ferran, 2017. Sen2Cor for sentinel-2. In: Bruzzone, Lorenzo, Bovolo, Francesca, Atli Benediktsson, Jon (Eds.), Image and Signal Processing for Remote Sensing XXIII. Image and Signal Processing for Remote Sensing. Warsaw, Poland, 2017. SPIE, p. 3. Available online at: https://www.spiedigitallibrary.org/conference-proceedings-of-spie/10427/2278218/Sen2Cor-for-Sentinel-2/10.1117/12.2278218.full.

Mananze, Sosdito, Pôças, Isabel, Cunha, Mário, 2020. Mapping and assessing the dynamics of shifting agricultural landscapes using google earth engine cloud computing, a case study in Mozambique. Rem. Sens. 12 (8), 1279. https://doi.org/10.3390/rs12081279.

Miranda, Nuno, Meadows, P.J., 2012. Radiometric Calibration of S-1 Level 1 Products Generated by the S-1 IPF. Available online at:, first ed. ESA.

Mugume, I., 2022. The Seasonal Rainfall Outlook for June to August 2022 over Uganda. Uganda National Meteorological Authority (UNMA). Available online at: https://www.unma.go.ug/seasonal-forecasts/. (Accessed 26 June 2023).

Nguyen, Minh, Baez-Villanueva, Oscar, Bui, Duong, Nguyen, Phong, Ribbe, Lars, 2020. Harmonization of Landsat and Sentinel 2 for crop monitoring in drought prone areas: case studies of ninh thuan (Vietnam) and Bekaa (Lebanon). Rem. Sens. 12 (2), 281. https://doi.org/10.3390/rs12020281.

Pettorelli, Nathalie, Vik, Jon Olav, Mysterud, Atle, Gaillard, Jean-Michel, Tucker, Compton J., Stenseth, Nils Chr, 2005. Using the satellite-derived NDVI to assess ecological responses to environmental change. Trends Ecol. Evol. 20 (9), 503–510. https://doi.org/10.1016/j.tree.2005.05.011.

Poortinga, Ate, Tenneson, Karis, Shapiro, Aurélie, Nquyen, Quyen, Aung, San, Khun, Chishtie, Farrukh, Saah, David, 2019. Mapping plantations in Myanmar by fusing Landsat-8, Sentinel-2 and Sentinel-1 data along with systematic error quantification. Rem. Sens. 11 (7), 831. https://doi.org/10.3390/rs11070831.

Qiu, Shi, Zhu, Zhe, He, Binbin, 2019. Fmask 4.0: improved cloud and cloud shadow detection in Landsats 4–8 and Sentinel-2 imagery. Remote Sensing of Environment 231, 111205. https://doi.org/10.1016/j.rse.2019.05.024.

Rathcke, B., Lacey, E.P., 1985. Phenological patterns of terrestrial plants. Annu. Rev. Ecol. Syst. 16 (1), 179–214. https://doi.org/10.1146/ANNUREV.ES.16.110185.001143.

Reed, Bradley C., Brown, Jesslyn F., VanderZee, Darrel, Loveland, Thomas R., Merchant, James W., Ohlen, Donald O., 1994. Measuring phenological variability from satellite imagery. J. Veg. Sci. 5 (5), 703–714. https://doi.org/10.2307/3235884.

Reyer, Christopher P.O., Leuzinger, Sebastian, Rammig, Anja, Wolf, Annett, Bartholomeus, Ruud P., Bonfante, Antonello, et al., 2013. A plant's perspective of extremes: terrestrial plant responses to changing climatic variability. Global Change Biol. 19 (1), 75–89. https://doi.org/10.1111/gcb.12023.

Roy, D.P., Zhang, H.K., Ju, J., Gomez-Dans, J.L., Lewis, P.E., Schaaf, C.B., et al., 2016. A general method to normalize Landsat reflectance data to nadir BRDF adjusted reflectance. Remote Sensing of Environment 176, 255–271. https://doi.org/10.1016/j.rse.2016.01.023.

Roy, David P., Li, Jian, Zhang, Hankui K., Yan, Lin, Huang, Haiyan, Li, Zhongbin, 2017. Examination of Sentinel-2A multi-spectral instrument (MSI) reflectance anisotropy and the suitability of a general method to normalize MSI reflectance to nadir BRDF adjusted reflectance. Remote Sensing of Environment 199, 25–38. https://doi.org/10.1016/j.rse.2017.06.019.

Storey, James, Roy, David P., Masek, Jeffrey, Gascon, Ferran, Dwyer, John, Choate, Michael, 2016. A note on the temporary misregistration of Landsat-8 Operational Land Imager (OLI) and Sentinel-2 Multi Spectral Instrument (MSI) imagery. Remote Sensing of Environment 186, 121–122. https://doi.org/10.1016/j.rse.2016.08.025.

The World Bank, 2020. Agricultural land (% of land area). Available online at: https://climateknowledgeportal.worldbank.org/country/uganda/climate-data-historical. (Accessed 19 July 2023).
Vogels, Marjolein, Jong, Steven de, Sterk, Geert, Douma, Harke, Addink, Elisabeth, 2019. Spatio-temporal patterns of smallholder irrigated agriculture in the horn of Africa using GEOBIA and Sentinel-2 imagery. Rem. Sens. 11 (2), 143. https://doi.org/10.3390/rs11020143.
Vrieling, Anton, Leeuw, Jan De, Mohammed, Y. Said, 2013. Length of growing period over Africa: variability and trends from 30 Years of NDVI time series. Remote Sensing 5 (2), 982–1000. https://doi.org/10.3390/rs5020982.
Weather and Climate, 2023. Kamuli, Uganda climate. The global Historical weather and climate data. Available online at: https://tcktcktck.org/uganda/kamuli. (Accessed 19 July 2023).
White, Michael, Beurs, Kirsten, Didan, K.A.M.E.L., Inouye, David, Richardson, Andrew, Jensen, Olaf, et al., 2009. Intercomparison, interpretation, and assessment of spring phenology in North America estimated from remote sensing for 1982-2006. Global Change Biol. 15 (10), 2335–2359. https://doi.org/10.1111/j.1365-2486.2009.01910.x.
White, Michael A., Hoffman, Forrest, Hargrove, William W., Nemani, Ramakrishna R., 2005. A global framework for monitoring phenological responses to climate change. Geophys. Res. Lett. 32 (4) https://doi.org/10.1029/2004GL021961.
White, Michael A., Thornton, Peter E., Running, Steven W., 1997. A continental phenology model for monitoring vegetation responses to interannual climatic variability. Global Biogeochem. Cycles 11 (2), 217–234. https://doi.org/10.1029/97GB00330.
Xu, Dandan, Guo, Xulin, 2014. Compare NDVI extracted from Landsat 8 imagery with that from Landsat 7 imagery. AJRS 2 (2), 10. https://doi.org/10.11648/j.ajrs.20140202.11.
Yin, Feng, Lewis, Philip E., Gómez-Dans, Jose L., 2022. Bayesian atmospheric correction over land: Sentinel-2/MSI and Landsat 8/OLI. Geosci. Model Dev. (GMD) 15 (21), 7933–7976. https://doi.org/10.5194/gmd-15-7933-2022.
Zeng, Linglin, Wardlow, Brian D., Xiang, Daxiang, Hu, Shun, Li, Deren, 2020. A review of vegetation phenological metrics extraction using time-series, multispectral satellite data. Remote Sensing of Environment 237, 111511. https://doi.org/10.1016/j.rse.2019.111511.
Zhang, Yili, Gao, Jungang, Liu, Linshan, Wang, Zhaofeng, Ding, Minjung, Yang, Xuchao, 2013. NDVI-based vegetation changes and their responses to climate change from 1982 to 2011: a case study in the Koshi River Basin in the middle Himalayas. Global Planet. Change 108, 139–148. https://doi.org/10.1016/j.gloplacha.2013.06.012.
Zhu, Zhe, Wang, Shixiong, Woodcock, Curtis E., 2015. Improvement and expansion of the Fmask algorithm: cloud, cloud shadow, and snow detection for Landsats 4–7, 8, and Sentinel 2 images. Remote Sensing of Environment 159, 269–277. https://doi.org/10.1016/j.rse.2014.12.014.
Zupanc, A., 2017. Improving Cloud Detection with Machine Learning.